



HAL
open science

Curvature Wavefront Sensing: Simple, Elegant, and Efficient

Olivier Lai, Mark Chun

► **To cite this version:**

Olivier Lai, Mark Chun. Curvature Wavefront Sensing: Simple, Elegant, and Efficient. The WSPC Handbook of Astronomical Instrumentation, 2, WORLD SCIENTIFIC, pp.187-203, 2021, 10.1142/9789811203787_0010 . hal-03570898

HAL Id: hal-03570898

<https://cnrs.hal.science/hal-03570898>

Submitted on 13 Feb 2022

HAL is a multi-disciplinary open access archive for the deposit and dissemination of scientific research documents, whether they are published or not. The documents may come from teaching and research institutions in France or abroad, or from public or private research centers.

L'archive ouverte pluridisciplinaire **HAL**, est destinée au dépôt et à la diffusion de documents scientifiques de niveau recherche, publiés ou non, émanant des établissements d'enseignement et de recherche français ou étrangers, des laboratoires publics ou privés.

Chapter 1

Curvature Wavefront Sensing: simple, elegant and efficient

Olivier Lai*¹ and Mark Chun²

¹ *Laboratoire Lagrange,
Université de Nice-Sophia Antipolis, CNRS,
Observatoire de la Côte d'Azur, BP 4229
06304 Nice cedex 4, France,*

² *Institute for Astronomy,
University of Hawaii,
640 N. Aohoku Place,
Hilo, HI 96720, United States*

Curvature sensing is a very simple and elegant method to measure the Laplacian of the wavefront, based on the conservation of flux irradiance. Its implementation does not require any special optical components and as it is a direct measure of intensity in defocused images, photodiodes or other read-noise-less detectors can be used. Because it is a differential measurement, it is insensitive to biases and internal errors. Coupled with bimorph mirrors, it provides the most efficient type of adaptive optics and is perfectly suited to the spatial spectrum of atmospheric turbulence. Nonetheless there are some drawbacks to curvature wavefront sensing, most notably due to spatial aliasing and dynamic range.

1. Out-of-focus images

Amateur astronomers defocus their telescopes to collimate them¹ and traditionally, physicists and optical scientists have used out-of-focus images to assess the aberrations of an optical system. As shown in Fig. 1, the out-of-focus images for a circular pupil should be round and evenly illuminated. Deviation to either the shape or the illumination are due to phase aberrations. In fact it is possible to identify and estimate aberrations using defocused images because each Zernike aberration produces a well identified pattern when viewed out of focus. For example, astigmatism elongates the defocused image symmetrically,² while coma produces an asymmetric elongation³ as shown in Fig. 2. François Roddier developed and formalized this primarily qualitative idea using the irradiance transport equation in 1988⁴ and laid the foundations for curvature wavefront sensing.

*olivier.lai@oca.eu

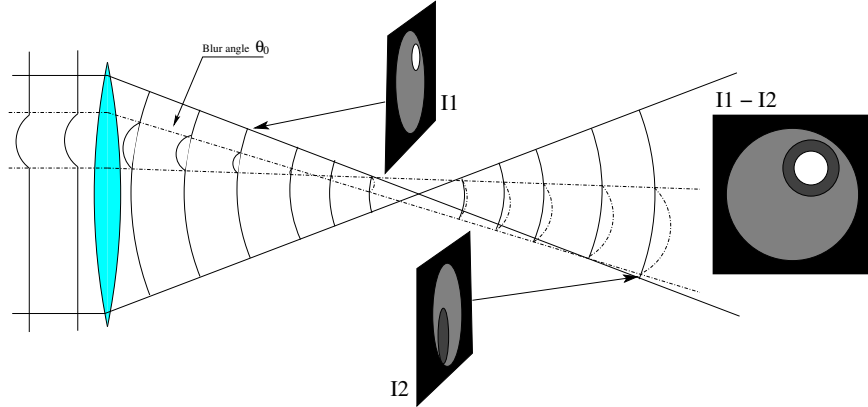


Fig. 1. A geometrical optics diagram showing the principle of curvature adaptive optics. A region of the wavefront with some curvature will focus ahead of the nominal focus. As it propagates, the phase aberration transforms into an intensity variation. In the out-of-focus planes, the intensity is proportional to the local curvature of the wavefront. The aberrations will focus closer to the pupil for a larger blur angle θ_0 (See sections 3.1 & 4.1 for details).

Because it is neither feasible nor practical to record the phase of electromagnetic waves at optical wavelengths, all the wavefront sensing methods need to transform a phase object into an intensity object, which can then be measured. This is either done by interferometric means or by using an optical element (such as a lenslet array or a pyramid) that transforms a function of the phase (usually some derivative) into an intensity function. Curvature sensing is based on the fact that where phase is introduced it has no effect on the intensity, but as the beam propagates, the phase deforms the beam and naturally reveals itself as intensity fluctuations: where the beam converges, the intensity locally increases and conversely, beam divergence introduces a decrease in the local illumination. This behavior is described by the *irradiance transport equation*.⁵⁻⁷

2. Conservation of flux

Curvature wavefront sensing is based on the law of conservation of flux, which can be described in most general terms by the time-invariant irradiance transport equation. It simply states that the light energy is conserved as the beam propagates along its optical axis. Consider the wave $\psi(x, y, z) = [\sqrt{I(x, y, z)} \exp(-i\phi(x, y, z))]$, where $I(x, y, z)$ is the intensity distribution along the beam, and $\phi(x, y, z)$ is the phase. We can write the wavefront $W(x, y, z)$ in terms of the phase $\phi(x, y, z) = (2\pi/\lambda)W(x, y, z) = kW(x, y, z)$ with k the wavenumber. The irradiance transport equation can be written as:

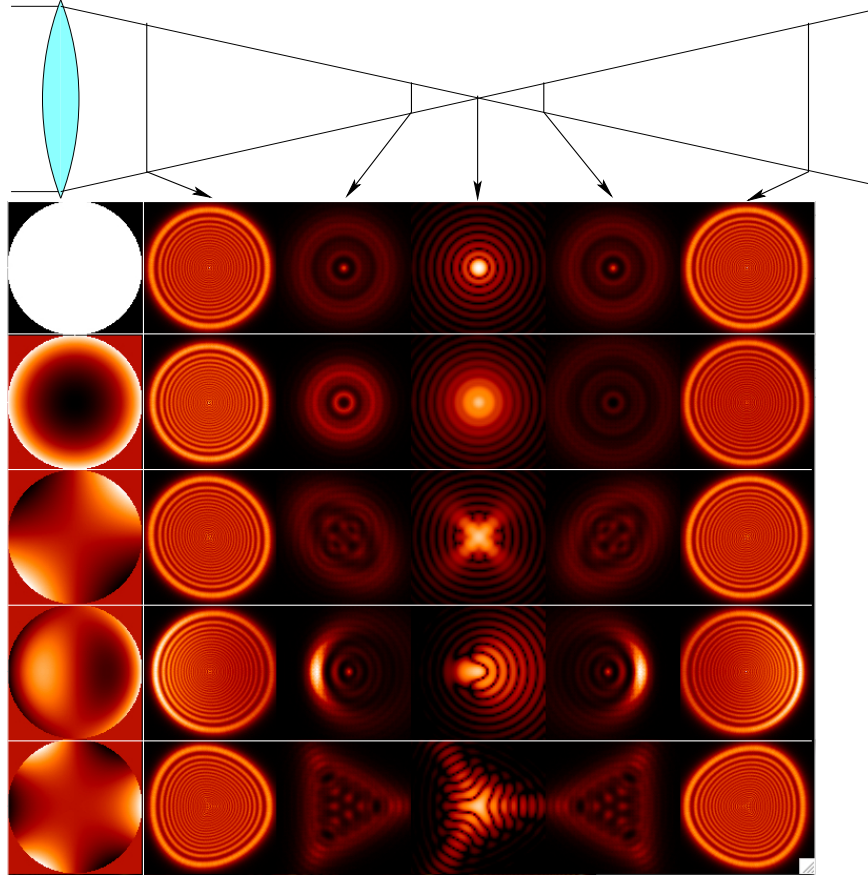


Fig. 2. The intensity distribution for various simple aberrations from pupil plane to focus.

$$\frac{\partial I}{\partial z} = -\vec{\nabla}(I \cdot \vec{\nabla}W) \quad (1)$$

$$= -(\vec{\nabla}I \cdot \vec{\nabla}W + I\nabla^2W), \quad (2)$$

where $\vec{\nabla}$ is the three-dimensional derivative operator $\vec{i}\partial/\partial x + \vec{j}\partial/\partial y + \vec{k}\partial/\partial z$, but let us restrict the beam propagation to the z axis such that $k_x, k_y \ll k_z$, so that we can simplify $\vec{\nabla}$ as $\vec{i}\partial/\partial x + \vec{j}\partial/\partial y$. Thus, ∇^2 is equal to $\partial^2/\partial x^2 + \partial^2/\partial y^2$ and is the Laplacian operator, tracing the curvature of the wavefront. Let us define the transmission function $P(x, y)$ of the pupil of the optical system; $P(x, y)$ equals one inside the pupil and zero outside. The illumination is uniform, equal to I_0 , inside the pupil. Therefore the gradient of the intensity $\vec{\nabla}I$ is equal to zero everywhere except at the pupil's edge, where it is given by:

$$\vec{\nabla}I = -I_0\vec{n}\delta_c, \quad (3)$$

where δ_c is a linear Dirac function on the edge of the pupil, and \vec{n} is a unit vector around the edge of the pupil (and pointing outwards). We can then rewrite Eq. (1) as:

$$\frac{\partial I}{\partial z} = \frac{\lambda}{2\pi} I (\delta_c \frac{\partial \phi}{\partial r} + \nabla^2 \phi) \quad (4)$$

because the dot product of \vec{n} and the azimuthal derivative of the wavefront is null. Finally, we can make the following simplifying assumption:

$$\frac{1}{I} \frac{\partial I}{\partial z} \simeq \frac{1}{I_0} \frac{\delta I}{\delta z} \quad (5)$$

$$\simeq \frac{2}{(z_1 - z_2)(I_{z_1} + I_{z_2})}, \quad (6)$$

where $I_0 = (I_{z_1} + I_{z_2})/2$. To further simplify the notation, let us assume that the two out-of-focus analysis planes are symmetrical around the pupil plane ($z_1 = -z_2$); we call the distance from focus to these planes the defocus length l , such that $z = f - l$. Lastly, we define a position vector ρ on the out-of-focus image, similar to r but scaled to the out-of-focus image $\rho = \mathbf{r} \times f/l$. Everything is in place to finally write down the curvature equation.

3. Curvature equation

The curvature equation is:

$$\frac{I_1(\mathbf{r}) - I_2(-\mathbf{r})}{I_1(\mathbf{r}) + I_2(-\mathbf{r})} = \frac{\lambda}{2\pi} \frac{f(f-l)}{l} \left[\nabla^2 \phi(\rho) - \delta_c \frac{\partial \phi}{\partial r} \right]_{\rho=\frac{r_f}{l}}. \quad (7)$$

Let us interpret this equation. The left hand side is the out-of-focus *contrast*, a normalized difference of intensity distributions in planes symmetrical around the focus; this is our measurement and it is equal to, on the right hand side, the Laplacian of the phase, i.e. its curvature (this is sometimes called the *lens* term). A differential equation of the form $\Psi = \nabla^2 \phi$ is called a Poisson equation. On the right hand side, there is also the radial derivative at the edge of the pupil (sometimes called the *prism* term), which provides the boundary conditions necessary to solve this differential equation; this is called a von Neumann boundary condition in that the constants of integration are specified as a derivative around the integration domain, as opposed to Dirichlet boundary conditions (that are in the form of the value of the function at the boundary to be integrated). Numerical techniques exist to solve Poisson equations with von Neumann boundary conditions, but in the case of curvature adaptive optics, this is not necessary as we will see in Sec. 5. The prism term allows the curvature sensor to be sensitive to Zernike polynomials that may have a zero curvature (such as tip, tilt or even astigmatism where $\partial^2 \phi / \partial x^2 = -\partial^2 \phi / \partial y^2$ everywhere on the pupil), but that displace or distort the out-of-focus beam, which is a consequence of a non-zero divergence (in the mathematical sense) of the intensity, ∇I , as shown on the third (and fifth) row of Fig. 2.

3.1. Optical gain

We note that the defocus length l appears in the denominator of the constants on the right hand side. This acts as an *optical gain*: the closer the analysis planes are to the focus, the stronger the measured signal for a given curvature. This can be understood physically by considering what happens to a phase defect of a given amplitude depending on whether it is very localized in the pupil (a high spatial frequency) or whether it extends over the entire pupil (low spatial frequencies), as shown in Fig. 3. Local defects have a large *blur angle*, θ_0 (Fig. 1) and will converge very rapidly (close to the pupil). By the time the light reaches focus, this light will mostly be scattered across the focal plane. A broad aberration (of the same amplitude) will have a small blur angle and there will be barely any intensity variation close to the pupil (large l). However, the shape of the PSF will be grossly modified, so sensitivity will be highest at small defocus lengths. The curvature sensor can thus be tuned to be sensitive to different spatial scales as well as for gain: putting the measurement planes far from focus increases the sensitivity to higher spatial frequencies at the expense of the low ones, while a high gain to low spatial frequencies can be achieved close to focus, at the expense of sensitivity to high spatial frequencies. Working close to focus means that the dynamic range is limited and measurements become non-linear when the amplitude of the phase defects becomes too large. This non-linearity is due to diffraction effects that are not included in the Curvature equation. The curvature sensor works well around its zero and is an ideal closed loop sensor, but in practice, an optimal defocus length needs to be determined, to maximize the sensitivity to the residual phase aberrations while remaining in the linear regime. In its original inception, it was conceived that the optical gain could gradually be increased as the adaptive optics loop closed and the phase excursions amplitude decreased. This has never been needed or implemented thanks to the stability of closed loop systems.

4. Development and implementations

The curvature wavefront sensor was first implemented on the UH-AO system by François Roddier and collaborators in 1991.⁸ It was a 13 element system that implemented a modulation of the defocus length using a vibrating membrane mirror at a focal plane. When the membrane is flat, the pupil is re-imaged on the lenslet array, and as it vibrates and changes its radius of curvature, it re-images out-of-focus planes conjugated to different distance from the pupil ($= f - l$) at constant magnification on the lenslet array. Thus the stronger the amplitude, the smaller l is and the stronger the optical gain. Each lenslet was coupled to an avalanche photodiode in photon-counting mode, and synchronous detection with the membrane mirror was used to integrate counts in the intra- and extra- focal images. An elegant design feature of this implementation is that the measurement becomes differential and is thus insensitive to defects and biases within the sensor (e.g. variable transmission or

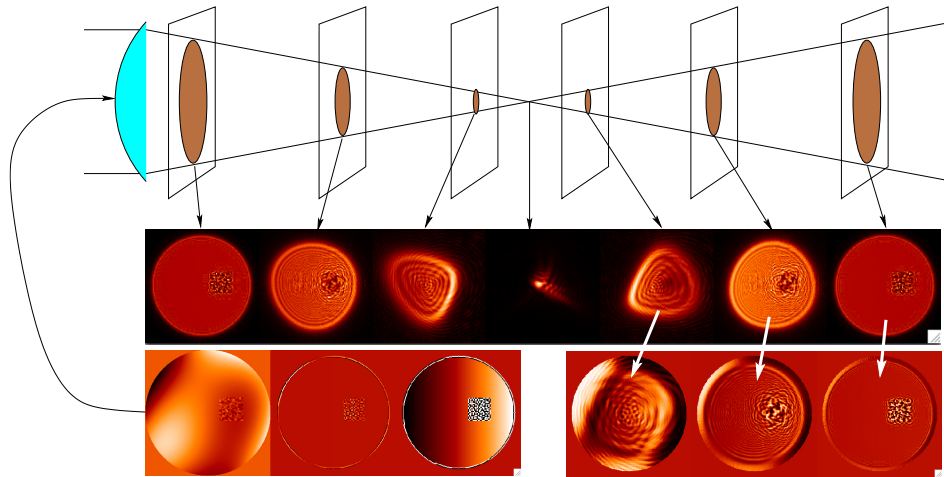


Fig. 3. The sensitivity of a curvature sensor as a function of its optical gain. *Bottom left panel:* The phase (left image) is fed through the optical system. The central and right-hand images of the bottom left panel show, respectively, the Laplacian at full scale and with a stretched scale to enhance the contrast. Note that the phase is composed of low spatial frequencies as well as a square of high spatial frequencies close to the center. *Top panel:* Schematic diagram showing seven positions at which the intensity distribution is computed and displayed in the middle panel, as indicated by the arrows. These positions represent the situation close to the pupil (left and right extreme images), in the linear range, close to the focus, and at the focus (central image). *Middle panel:* Intensity distributions at the indicated positions. *Bottom right panel:* the contrast is displayed for three of the images in the central panel. Proximity to the pupil improves sensitivity to high spatial frequencies at the expense of low spatial frequencies. Too close to the focus and non-linearities due to the pupil's edge diffraction are introduced. Thus the linear range (and optimal optical gain - middle of bottom right panel) depends on the defocus length.

fiber-APD coupling). At the same time, this design allows the defocus length to be modulated and optimized without altering any optical alignments or components. Most (if not all) operational curvature adaptive optics systems have used this focal plane vibrating membrane mirror design. Because such mirrors are acoustically driven by means of an acoustic loudspeaker, curvature sensors emit a characteristic high-pitched pure sine wave sound.

4.1. Defocus length

The defocus distance has to be chosen so that the geometrical approximation of Eq. (7) remains valid. Thus l has to be chosen such that the diffraction or speckle blur produced at the position of the defocused image remains small with respect to the wavefront fluctuations we want to measure, in other words, the size of the subapertures, d . At the defocus plane, the size of the subaperture is ld/f , and the

blur size will be $(f - l)\theta_0$, so must satisfy the following condition:

$$(f - l)\theta_0 \leq ld/f \quad (8)$$

$$l \geq \frac{f}{1 + d/(f\theta_0)} \quad (9)$$

For large blur angles, l tends to f (i.e. close to the pupil), but when θ_0 is small compared to the f-ratio of the subapertures beams, d/f , the expression for the defocus length can be simplified to:

$$l \geq \theta_0 \frac{f^2}{d} \quad (10)$$

If the subaperture size d is larger than r_0 , then the blur angle is given by λ/r_0 such that $l \geq \lambda f^2/(r_0 d)$. This is the behavior expected for a low order system. However as the loop closes the effective r_0 increases and the diffraction of the lenslets (of size λ/d) becomes dominant. The sensor can bootstrap on its own correction and the defocus length can be reduced to $l \geq \lambda f^2/d^2$. This condition is very close to the near field approximation^a, so we conclude that the optimal defocus length occurs at the shortest distance from focus where diffraction effects do not degrade the measurements.

Another possible implementation of the curvature sensor, if used at fixed defocus length (so possibly more apt for a laboratory setting) is to simply use a beamsplitter to re-image the intra- and extra-focal images on the same detector. Although the size of the subapertures can be optimized by binning, the sensor will remain most sensitive to a given blur angle since l cannot (easily) be varied. What is gained here in ease of implementation is paid for in post-processing: the images have to be normalized, scaled and co-aligned accurately. Furthermore, any aberrations introduced after the beam is separated will be interpreted as a spurious bias signal.

5. Advantages of Curvature AO

5.1. *Bimorph mirrors*

So far we have only discussed the principles and implementations of the curvature wavefront *sensor*, but the real advantage of this method comes from the coupling of this sensor with a bimorph mirror. Such a mirror is composed of an electrode pattern sandwiched between two wafers of oppositely polarized piezoelectric ceramic, and a grounding electrode around each (Fig. 4 left). When a voltage is applied to one electrode, the piezo-ceramic on one side will expand while the one on the other side will contract, bending the surface at the location of the electrode (Fig. 4 right).

In fact, the surface will bend with a radius of curvature:⁹

$$R_{xy} = \frac{V_z d_{xy}}{t^2}, \quad (11)$$

^aFor a parallel beam, the Fresnel distance before which diffraction effects appear is equal to $L \leq d^2/\lambda$.

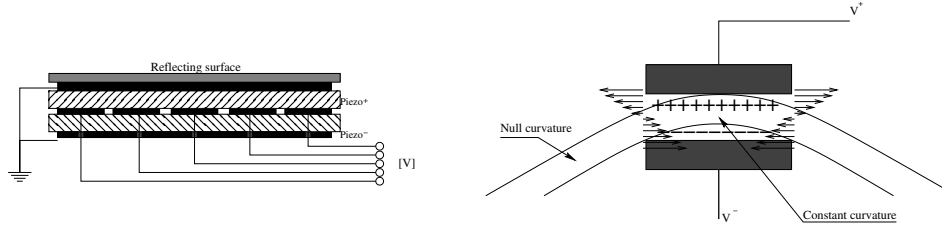


Fig. 4. Left: An electrode pattern is sandwiched between two oppositely polarized piezoelectric wafers (hatched) with a grounding electrode on the outside. Right: when an electric field is applied across the piezo ceramic, it expands or contracts, generating constant curvature on the electrode pattern.

where V_z is the voltage across the electrode of thickness t and d_{xy} is the transverse element of the piezoelectric tensor \mathbf{d}_{ij} . Thus, if the electrode pattern matches the wavefront sensor lenslet pattern, the sensor measures exactly what the mirror is capable of producing (see Fig. 5). The theoretical interaction matrix for such a system is purely diagonal (Fig. 7, left) and is trivial to invert. As such it provides the least amount of reconstruction noise, as there are no poorly conditioned modes. In practice, there is a piston term produced by the edge electrodes which is invisible to the sensor, but it is easy to filter out and has no effect on the final image (nonetheless care needs to be taken if the adaptive optics system is to be used in interferometry, e.g. the MACAO systems^{10,11} on VLTI at ESO¹²). This also means that in principle, there is no reconstruction required and each electrode-lenslet channel can be controlled independently. Thus, in theory the adaptive optics control loop could be implemented analogically;⁸ although this has never been tried in practice, it remains an interesting implementation in applications where bandwidth is of utmost importance. However, due to imperfect materials of the mirror, connecting wires, and diffraction in the sensor, there is usually some level of crosstalk between electrodes and neighboring lenslets and the interaction matrix does contain some non-zero non-diagonal terms (see Figs. 5 and 7, right). A standard inversion scheme allows reconstruction of the mirror voltage vector but with minimal noise propagation due to the good conditioning of the interaction matrix.

5.2. Avalanche PhotoDiodes

The use of avalanche photodiodes in the wavefront sensor is also advantageous, as there is obviously no read noise. Also, because the sensor only measures the intensity within a lenslet, there is no need to form an image and read multiple pixels for each measurement. The wavefront sensor can thus be set to work at the highest frame rate available and the photon noise can be averaged numerically in the closed loop integrator by choosing the appropriate loop gain. This simplifies the control of the loop, as there is no need to change the frame rate to optimize the SNR at each read: the sensor is run at its maximum available frequency but a low

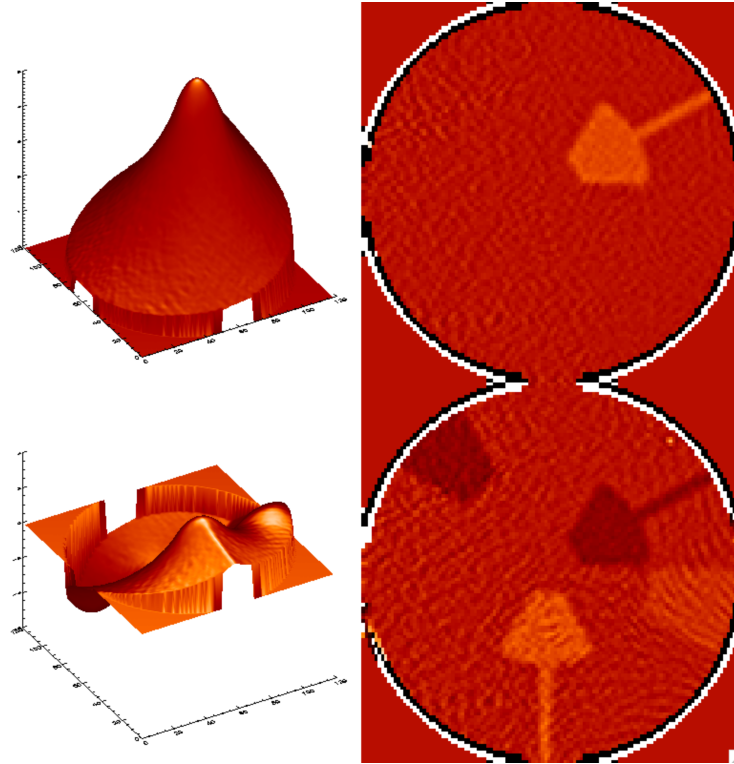


Fig. 5. Left: the phase produced by actuating one electrode (top) and four of them (bottom). Right: the associated Laplacian of the phase maps reveals the electrode pattern. The junction wires are visible and are in part responsible for the cross-talk in and non-diagonal elements of the interaction matrix.

gain value ensures that the overshoot of the closed loop transfer function is kept to a minimum.

5.3. *Strehl efficiency*

Finally, the curvature sensor is ideally suited to measure atmospheric turbulence. In the case of Kolmogorov turbulence, the amplitude of the spatial spectrum of the phase varies as $k^{-11/6}$ (k being the spatial frequency). Curvature is the second derivative of the phase, so the amplitude of the spectrum of curvatures varies as $k^{+1/6}$ (differentiating a function multiplies the amplitude of its Fourier transform by the spatial frequency k , but curvature is the second order derivative, so multiplies the amplitude spectrum by k^2). This means that the curvature spatial spectrum is almost flat, thus measurements are uncorrelated. This in turn implies that each electrode-lenslet channel is statistically (almost) independent from the others and corrects the phase deformation optimally on a per-actuator basis. This is of course important in astronomical applications where each photon matters. Refs. 13 and

14 studied the *efficiency* of adaptive optics systems; it is defined as the ratio of the effective number of ideal modes corrected to the actual number of actuators in the system, $q = N_{eff}/N_{act}$. Fewer larger subapertures at equivalent correction (N_{eff} constant) improves the limiting magnitude (or reduces laser power requirements), a desirable feature in astronomical applications where photons are precious. But AO systems with fewer subapertures and pixels are not only less expensive to build and to maintain, they also benefit from reduced calibration and reconstruction errors; the good match between what the sensor measures and what the mirror can produce means that interaction matrices are diagonal, leading to reduced invisible (or low sensitivity) modes and improved noise propagation. Maybe for all these reasons, curvature AO systems are found to have substantially higher efficiencies than Shack-Hartmann ones (see Fig. 6. It is unfortunate that these studies were carried out before pyramid sensors started delivering results, as it would be most interesting to see where the pyramid sensor lies on such a family of curves.

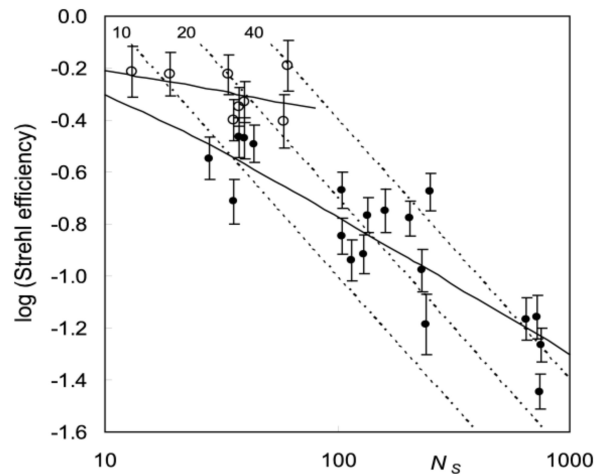


Fig. 6. The Strehl efficiency for curvature AO systems (open circles) and Shack Hartmann ones (filled circles), as a function of number of subapertures from Ref. 14. The dotted lines represent isovariances labelled with their effective number of subapertures $N_{eff} = 10, 20, 40$.

6. Disadvantages of Curvature sensing

6.1. Null sensor

Due to its limited linear range, curvature sensing is effective as a null sensor. However, as such, it is difficult to use in applications working off-null, for example to include so-called “centroid offsets” to compensate for static aberrations, or in

GLAO^b, MOAO^c or open loop AO^d. To increase the dynamic range, the optical gain can be reduced by increasing the defocus length, but there is nonetheless an intrinsic blur and an increase in aliasing in working far off null. This is best understood if we think of the effect of a tilt on the wavefront: if left uncorrected, higher spatial frequency defects will not line up on the contrast image (as they will be offset from one another due to the original tilt), and will produce a signal with even more apparent high spatial frequencies. In the example shown in Fig. 1, the contrast image would show an elliptical zone rather than a circular one if the two defocused images were not aligned.

6.2. *Tip-tilt sensing noise*

The edge subapertures provide the radial derivative around the pupil. If these subapertures were to line up precisely with the edge of the pupil, and there was no tip-tilt, no flux would reach them, which in practice can cause some difficulties. For practical reasons, the edge subapertures intersect some of the pupil so that each subaperture covers the same illuminated area and correspondingly has the same Signal-to-Noise ratio when there is no input perturbation. This reduces the sensitivity of the curvature sensor to modes with non-zero phase divergence, of which tip and tilt are the first and carry the largest variance. Unevenly illuminated subapertures may actually be preferable, but an appropriate weighting scheme has to be used in the reconstructor.

6.3. *Aliasing*

The curvature sensor's best known disadvantage is its sensitivity to aliasing. Aliasing is the spurious interpretation of high spatial frequencies (above the cut-off spatial frequency $k_c = 1/2l_{act}$) folded back onto the low order modes that are being measured; these high spatial frequency are propagated through the reconstructor and appear as low order modes in the correction. The amplitude of the spectrum of phase curvatures varies as $k^{+1/6}$, which means that there is a slight increase in curvature signal at smaller and smaller spatial scales (until the inner scale). Although on average this signal is of zero mean, its variance increases with decreasing spatial scale. These high frequency curvature signals are averaged inside the lenslets making the measurements, but still produce an instantaneous (spurious) signal across those (low order) subapertures. The aliasing error can be decreased by decreasing the defocus length, but when the blur angle associated with these high spatial frequencies starts to introduce diffraction, these can lead to a non-linear response of the sensor, which compounds the aliasing problem (Fig. 7, right). There is no simple analytical way to compute the aliasing error, but Monte Carlo simulations

^bSee Chapter 17 of this Volume.

^cSee Chapter 18 of this Volume.

^dFor example, see Chapter 14 of this Volume.

carried out by Ref. 15 show that it is approximately double that of Shack-Hartmann systems.

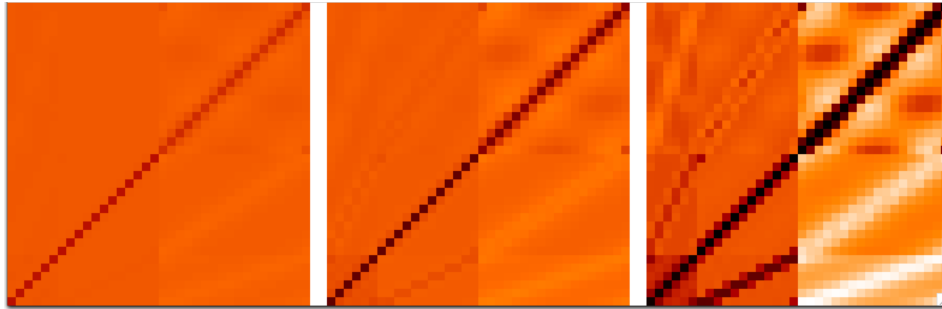


Fig. 7. Interaction matrices for a 36 electrode system arranged in three rings of (6,12,18), with WFS vectors shown as columns and mirror electrodes as rows. All WFS responses are shown at the same scale for a normalized input electrode voltage vector. Left: at large defocus distances, the sensor is well behaved and the matrix is diagonal, but the response for a normalized signal is weak. Middle: optimal tuning of the wavefront sensor, with a strong signal but limited cross talk (non-diagonal terms). Right: the optical gain is too strong, and diffraction is causing cross-talk between subapertures.

Increasing the number of subapertures on a curvature AO system improves the aliasing error and forces the sensor to work at greater defocus lengths. In this case, it is the sensitivity to low order modes which is decreased because they suffer from low optical gain. Unless clever techniques such as multiple defocus lengths (see Sec. 8.4) are used, this sets an upper limit to the order of curvature AO systems.

7. Astronomical curvature AO systems

There are a handful of highly productive curvature AO systems around the world, presented non-exhaustively in Table 1. Modern developments in AO have focused on increasing the field of view (GLAO, MOAO) and also on increasing the on-axis Strehl of SCAO systems for high dynamic range imaging. A requirement for wide field AO is a wavefront sensor with large dynamic range, at odds with the curvature null-sensing regime. The low sensitivity to low spatial frequencies for very high order systems is a drawback of curvature sensing for high dynamic range applications, but can be compensated for by a “woofer-tweeter” architecture. Although pyramid sensors appear extremely well suited for the high order sensing, long defocus length curvature remains an attractive possibility.

Table 1. Curvature AO systems.

System	Telescope	Degrees of Freedom	Year of operation
UHAO13 ^{8,16}	CFHT, UKIRT, UH88	13	1994, 1995, 1996 \mapsto 1998
PUEO ¹⁷	CFHT	19	1996 \mapsto 2012
UHAO36/Hokupa'a ^{18,19}	CFHT, Gemini	36	1997, 1999 \mapsto 2001
AO36 ^{20,21}	Subaru	36	2002 \mapsto 2008
MACAO VLTI ^{10,11}	ESO VLT	60	2003 \mapsto present
Sinfoni ²² /CRIRES ²³	ESO VLT	60	2003 \mapsto present
Hokupa'a ⁸⁵ ²⁴	Gemini N, AEOS	85	2001 \mapsto 2004, 2008 \mapsto present
NICI ^{25,26}	Gemini S	85	2007 \mapsto 2013
AO188 ^{27,28}	Subaru	188	2008 \mapsto present
T3PWFS ²⁹	WHT	153	2017 \mapsto present

8. Recent Advances in Curvature AO

8.1. Use of CCDs

Avalanche Photodiodes are ideal detectors due to the lack of read noise, low dark currents and high quantum efficiencies. Nonetheless they are expensive, and actively quenched APDs have been known to fail. In an effort to lower the cost of curvature AO systems, MIT-Lincoln Labs in collaboration with ESO developed a CCD detector specifically for curvature sensing, the CCID-35. These detectors are composed of light-sensitive “super-pixels”, surrounded by a storage area on either side. As the membrane mirror scans the defocused pattern on each side of focus, the charges are sent back and forth from the super-pixel to each storage area, so that the counts for the intra- and extra focal images are co-added, but kept separate. The detector is read at a chosen frame rate which is a multiple of the membrane mirror frequency, so that the read noise is only incurred once. The optical fibers from the lenslet array can be terminated in a V-groove arrangement that matches the detectors super-pixel pattern, making it easy to match the round geometry of the pupil and subapertures to the the square geometry of CCD pixels.

Such a camera was tested with success on the PUEO adaptive optics system at CFHT.³⁰ The occurrence of read noise implies that the frame rate has to be adapted to optimize the SNR at each read, making operations more cumbersome, but the performance was otherwise comparable to the APDs, making such a system perfectly useable for high order curvature adaptive optics.

EMCCDs can also potentially be used in photon counting mode to replace APDs. Although the excess noise ($= \sqrt{2}$) is equivalent to a drop in throughput of 50%, its implementation is simpler than a typical APD-based curvature wavefront sensor, where the APDs are fed by fibers behind a lenslet array. The coupling between all these elements lowers the throughput to a point where these two approaches may be equivalent in noise.

8.2. Possibility of single out-of-focus image

The idea of using a single out-of-focus image is not new,³¹ but there is a degeneracy on the sign of the phase when the complex amplitude is sought from an intensity measurement, because the intensity is the modulus *squared* of the Fourier transform of the input complex amplitude. This is the reason why two images (one inside of focus, the other outside of it) are needed; namely, to identify the sign of aberrations that can be described by even functions, which produce centro-symmetric intensity distributions (e.g. focus, spherical aberration, etc.).

However, there are simple tricks that break down this degeneracy and can be used to lift this ambiguity. For example, if the pupil function is assumed to be uniform (neglecting scintillation) and made asymmetric, then it is possible to infer the sign of the phase with a single defocused image. In essence, this is equivalent to setting $z_2 = 0$ (and $I_{z_2} = I_0$) in Eq. (5), with an added constraint to make the transmission function $P(x, y)$ an odd function.

8.3. Spatial filtering

In the same way that a spatial filter at the entrance of a Shack-Hartmann wavefront sensor can reduce the aliasing,³² a similar device could be used to reduce the aliasing of a curvature sensor. A spatial filter/field stop could easily be implemented in the intermediate focal plane of the membrane mirror. Removing the high spatial frequencies by an optical filter essentially removes the light with too high a blur angle from the sensor and introduces an uneven illumination over the sensor. The size of the spatial filter should be λ/l_{act} where l_{act} is approximately the size of the electrodes. For systems optimized for the near infrared with large electrodes, where the potential for improvement due to reduced aliasing is the largest, the throughput through a spatial filter at the shorter wavefront-sensing wavelength would be very small. Conversely, high order systems, where the light losses through a spatial filter would be less, are less affected by aliasing and are dominated by low spatial frequency sensitivity. However, if the wavefront sensing were to be carried at longer wavelengths, or for a high order system producing reasonable correction at visible wavelengths, this improvement should prove beneficial to curvature, as it has been demonstrated to be in Shack-Hartmann sensors for high dynamic range AO systems. But in practice, the gain of anti-aliasing optical filtering in curvature sensing remains an open question.

8.4. Multiple defocus length

To address the issue raised in Sec. 6.3 regarding the loss of sensitivity to low spatial frequencies of a high order curvature AO system, an ingenious solution was found by O. Guyon^{33,34} and implemented in Subaru Telescope's AO188 system. Instead of driving the membrane mirror to a sine (or square) wave of a given amplitude, the membrane mirror is modulated to produce a two-step function (or approximation

thereof). In doing so, two different defocus lengths are produced. Synchronous detection allows integration of counts for large intra-focus, small intra-focus, small extra-focus and large extra-focus intensities. For the short defocus distances, measurements are effectively convolved with a broad filter to decrease the effective number of subapertures and reduce the sensitivity to diffraction.

Although it is not trivial to drive a membrane mirror with a complex output off its resonant frequency, Subaru's AO188 is currently the curvature system with the highest number of degrees of freedom used routinely in astronomy, and its performance demonstrates that this method is effective.

8.5. Non-linear curvature sensing – *n*lCWFS

Ref. 35 extended the idea of using 4 defocus planes (Fig. 8), combining it with a Phase Diversity scheme, using the Gershberg-Saxton algorithm, selected for its simplicity and flexibility. The non-linear Curvature Wavefront Sensor (*n*lCWFS) is computationally intensive for real time applications, as the GS algorithm is iterative and the phase also needs to be unwrapped, but it can be linearized when phase excursions are small, allowing one to bypass the non-linear reconstruction. Curiously, the *n*lCWFS sensitivity is improved when a known aberration is added to the beam, as the diffraction pattern around the pupil from a very clean wavefront otherwise dominates the signal and reduces its sensitivity. Although showing great promise from a theoretical standpoint, to our knowledge the *n*lCWFS has not yet been used in operational astronomical AO systems.

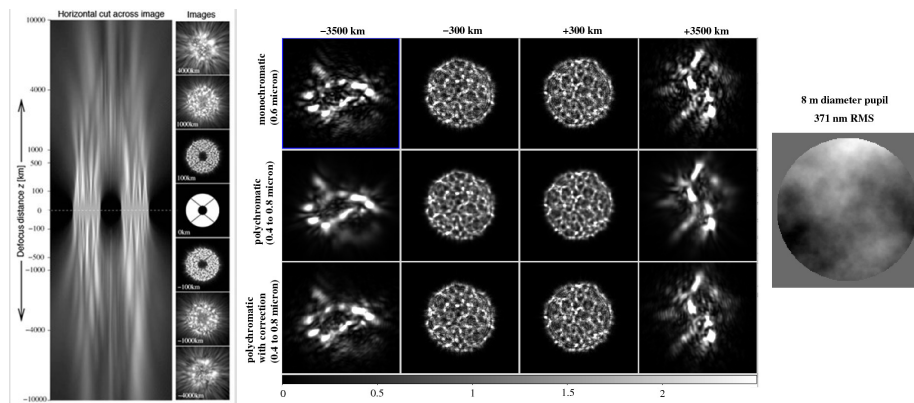


Fig. 8. Left: A transverse image of the illumination as a function of defocus distance, from simulations by Olivier Guyon. Middle panel: Top, Simulated frames obtained by the *n*lCWFS in monochromatic light; middle, in polychromatic light with no chromatic compensation; and bottom, in polychromatic light with chromatic compensation. The wavefront error across the 8 m diameter pupil used for this simulation is shown in the right-hand panel, from Ref. 35.

Curvature adaptive optics is currently not as widespread as other techniques, most likely because it is difficult to extend beyond single conjugate AO, and due

to the limited linear range of curvature sensing.^{36,37} However, an extension of curvature sensing, the “Two Pupil Plane Position Wavefront Sensor” (T3PWFS),³⁸ has recently been deployed at the William Herschel Telescope.²⁹

References

1. G. Seronik. No tools telescope collimation, (2014). <http://garyseronik.com/no-tools-telescope-collimation/>.
2. R. Wilson. Procedures and formulae for the adjustment of telescopes and analysis of their performance. memorandum, ESO Telescope Project Division, Garching bei München, Germany’, (1980).
3. A. Behr, A proposal for the alignment of large telescopes, *Astron. Astrophys.* **28**, 355 (Nov., 1973).
4. F. Roddier, Curvature sensing and compensation: a new concept in adaptive optics, *Applied Opt.* **27**, 1223–1225, (1988). doi: 10.1364/AO.27.001223.
5. M. Reed Teague, Deterministic phase retrieval: a green’s function solution, *Journal of the Optical Society of America (1917-1983)*. **73**, 1434, (1983).
6. N. Streibl, Phase imaging by the transport equation of intensity, *Optics Communications*. **49**, 6–10, (1984). doi: 10.1016/0030-4018(84)90079-8.
7. F. Roddier, Wavefront sensing and the irradiance transport equation, *Applied Opt.* **29**, 1402–1403, (1990). doi: 10.1364/AO.29.001402.
8. F. Roddier, M. Northcott, and J. E. Graves, A simple low-order adaptive optics system for near-infrared applications, *Publ. Astron. Soc. Pacific*. **103**, 131–149, (1991). doi: 10.1086/132802.
9. R. Tyson, *Principles of Adaptive Optics*. (Academic Press, Inc., 1250 Sixth Avenue, San Diego, CA92101, 1991).
10. R. Arsenault, J. Alonso, H. Bonnet, J. Brynnel, B. Delabre, R. Donaldson, C. Dupuy, E. Fedrigo, J. Spyromilio, T. Erm, J. Farinato, N. Hubin, L. Ivanescu, M. Kasper, S. Oberti, J. Paufique, S. Rossi, S. Tordo, S. Stroebele, J.-L. Lizon, P. Gigan, F. Poulard, F. Delplancke, A. Silber, M. Quattri, and R. Reiss, Macao-vlti first light: adaptive optics at the service of interferometry, *The Messenger*. **112**, 7–12, (2003).
11. R. Arsenault, R. Donaldson, C. Dupuy, E. Fedrigo, N. N. Hubin, L. Ivanescu, M. E. Kasper, S. Oberti, J. Paufique, S. Rossi, A. Silber, B. Delabre, J.-L. Lizon, and P. Gigan. Macao-vlti adaptive optics systems performance. In eds. D. Bonaccini Calia, B. L. Ellerbroek, and R. Ragazzoni, *Advancements in Adaptive Optics*, vol. 5490, *Proc. SPIE*, pp. 47–58, (2004). doi: 10.1117/12.552548.
12. L. Ivanescu, R. Arsenault, E. Fedrigo, M. E. Kasper, S. Oberti, J. Paufique, and S. Stroebele. Macao-vlti piston issue: achieving the interferometry requirements. In eds. D. Bonaccini Calia, B. L. Ellerbroek, and R. Ragazzoni, *Advancements in Adaptive Optics*, vol. 5490, *Proc. SPIE*, pp. 1534–1545, (2004). doi: 10.1117/12.551854.
13. F. Roddier, Maximum gain and efficiency of adaptive optics systems, *Publ. Astron. Soc. Pacific*. **110**, 837–840, (1998). doi: 10.1086/316194.
14. R. Racine, The strehl efficiency of adaptive optics systems, *PASP*. **118**, 1066–1075, (2006). doi: 10.1086/505990.
15. J. P. Véran. *Estimation de la réponse impulsionnelle et restauration d’image en optique adaptative, application au système d’optique adaptative du Télescope Canada-France-Hawaii*. PhD thesis, , École Nationale Supérieure des Télécommunications, France, (1997), (1997).
16. F. J. Roddier, J. Anuskiewicz, J. E. Graves, M. J. Northcott, and C. A. Roddier.

- Adaptive optics at the university of hawaii i: current performance at the telescope. In eds. M. A. Ealey and F. Merkle, *Adaptive Optics in Astronomy*, vol. 2201, *Proc. SPIE*, pp. 2–9, (1994).
17. F. Rigaut, D. Salmon, R. Arsenault, J. Thomas, O. Lai, D. Rouan, J. P. Véran, P. Giggan, D. Crampton, J. M. Fletcher, J. Stilburn, C. Boyer, and P. Jagourel, Performance of the canada-france-hawaii telescope adaptive optics bonnette, *Publ. Astron. Soc. Pacific*. **110**, 152–164, (1998). doi: 10.1086/316126.
 18. J. E. Graves, M. J. Northcott, F. J. Roddier, C. A. Roddier, and L. M. Close. First light for hokupa'a: 36-element curvature ao system at uh. In eds. D. Bonaccini and R. K. Tyson, *Adaptive Optical System Technologies*, vol. 3353, *Proc. SPIE*, pp. 34–43, (1998).
 19. J. E. Graves, M. J. Northcott, F. J. Roddier, C. A. Roddier, D. Potter, D. J. O'Connor, F. J. Rigaut, and M. R. Chun. First light for hokupa'a 36 on gemini north. In ed. P. L. Wizinowich, *Adaptive Optical Systems Technology*, vol. 4007, *Proc. SPIE*, pp. 26–30, (2000).
 20. H. Takami, N. Takato, T. Kanzawa, Y. Hayano, Y. Kamata, W. Gaessler, Y. Minowa, and M. Iye. The first light of subaru adaptive optics system. In eds. E. Vernet, R. Ragazzoni, S. Esposito, and N. Hubin, *European Southern Observatory Conference and Workshop Proceedings*, vol. 58, *European Southern Observatory Conference and Workshop Proceedings*, p. 427, (2002).
 21. H. Takami, N. Takato, Y. Hayano, M. Iye, S. Oya, Y. Kamata, T. Kanzawa, Y. Minowa, M. Otsubo, K. Nakashima, W. Gaessler, and D. Saint-Jacques, Performance of subaru cassegrain adaptive optics system, *Publ. Astron. Soc. Japan*. **56**, 225–234, (2004). doi: 10.1093/pasj/56.1.225.
 22. H. Bonnet, S. Ströbele, F. Biancat-Marchet, J. Brynnel, R. D. Conzelmann, B. Delabre, R. Donaldson, J. Farinato, E. Fedrigo, N. N. Hubin, M. E. Kasper, and M. Kissler-Patig. Implementation of macao for sinfoni at the vlt, in ngs and lgs modes. In eds. P. L. Wizinowich and D. Bonaccini, *Adaptive Optical System Technologies II*, vol. 4839, *Proc. SPIE*, pp. 329–343, (2003). doi: 10.1117/12.457060.
 23. J. Paufique, P. Biereichel, R. Donaldson, B. Delabre, E. Fedrigo, F. Franza, P. Giggan, D. Gojak, N. N. Hubin, M. E. Kasper, H.-U. Kaeufl, J.-L. Lizon, S. Oberti, J.-F. Pirard, E. Pozna, J. Santos, and S. Stroebele. Macao-crires: a step toward high-resolution spectroscopy. In eds. D. Bonaccini Calia, B. L. Ellerbroek, and R. Ragazzoni, *Advancements in Adaptive Optics*, vol. 5490, *Proc. SPIE*, pp. 216–227, (2004). doi: 10.1117/12.551675.
 24. M. J. Northcott, J. E. Graves, F. J. Roddier, and F. J. Rigaut. Design and performance of an 85-actuator curvature system. In ed. P. L. Wizinowich, *Adaptive Optical Systems Technology*, vol. 4007, *Proc. SPIE*, pp. 126–130, (2000).
 25. D. W. Toomey and C. Ftaclas. Near infrared coronagraphic imager for gemini south. In eds. M. Iye and A. F. M. Moorwood, *Instrument Design and Performance for Optical/Infrared Ground-based Telescopes*, vol. 4841, *Proc. SPIE*, pp. 889–900, (2003). doi: 10.1117/12.461099.
 26. M. Chun, D. Toomey, Z. Wahhaj, B. Biller, E. Artigau, T. Hayward, M. Liu, L. Close, M. Hartung, F. Rigaut, and C. Ftaclas. Performance of the near-infrared coronagraphic imager on gemini-south. In *Adaptive Optics Systems*, vol. 7015, *Proc. SPIE*, p. 70151V, (2008). doi: 10.1117/12.787683.
 27. Y. Hayano. Progress of the laser guide star adaptive optics at subaru telescope. In eds. T. Usuda, M. Tamura, and M. Ishii, *American Institute of Physics Conference Series*, vol. 1158, *American Institute of Physics Conference Series*, pp. 385–386, (2009). doi: 10.1063/1.3215902.

28. Y. Minowa, Y. Hayano, S. Oya, M. Watanabe, M. Hattori, O. Guyon, S. Egner, Y. Saito, M. Ito, H. Takami, V. Garrel, S. Colley, T. Golota, and M. Iye. Performance of subaru adaptive optics system ao188. In *Adaptive Optics Systems II*, vol. 7736, *Proc. SPIE*, p. 77363N, (2010). doi: 10.1117/12.857818.
29. C. Colodro-Conde, S. Velasco, J. J. Fernández-Valdivia, R. López, A. Oscoz, R. Reboló, B. Femenía, D. L. King, L. Labadie, C. Mackay, B. Muthusubramanian, A. Pérez Garrido, M. Puga, G. Rodríguez-Coira, L. F. Rodríguez-Ramos, J. M. Rodríguez-Ramos, R. Toledo-Moreo, and I. Villó-Pérez, Laboratory and telescope demonstration of the tp3-wfs for the adaptive optics segment of aoli, *Mon. Not. Royal Astron. Soc.* **467**, 2855–2868, (2017). doi: 10.1093/mnras/stx262.
30. O. Lai, J.-C. Cuillandre, K. K. Y. Ho, M. Baril, T. Benedict, J. Ward, J. Thomas, D. Salmon, C.-J. Lin, S.-Y. Wang, G. Luppino, R. Dorn, P. Puget, B. Burke, and J. Beletic, Flyeyes: A ccd-based wavefront sensor for pueo, the cfht curvature ao system, *Publ. Astron. Soc. Pacific*. **123**, 448–460, (2011). doi: 10.1086/659149.
31. P. Hickson, Wave-front curvature sensing from a single defocused image, *J. Opt. Soc. Am. A*. **11**, 1667–1673, (1994). doi: 10.1364/JOSAA.11.001667.
32. S. Thomas, L. Poyneer, D. Savransky, B. Macintosh, M. Hartung, D. Dillon, D. Gavel, J. Dunn, K. Wallace, D. Palmer, and R. De Rosa. Wavefront sensing and correction with the gemini planet imager. In *Adaptive Optics Systems III*, vol. 8447, *Proc. SPIE*, p. 844714, (2012). doi: 10.1117/12.926680.
33. O. Guyon, N. Arimoto, C. Blain, S. Colley, M. Eldred, M. Goto, M. Hattori, Y. Hayano, M. Iye, Y. Kamata, T. Kane, N. Kobayashi, M. Watanabe, Y. Minowa, S. Oya, Y. Saito, H. Takami, and N. Takato. Subaru telescope lgsao: overview of expected performance. In eds. D. Bonaccini Calia, B. L. Ellerbroek, and R. Ragazzoni, *Advancements in Adaptive Optics*, vol. 5490, *Proc. SPIE*, pp. 733–741, (2004). doi: 10.1117/12.551942.
34. O. Guyon, C. Blain, H. Takami, Y. Hayano, M. Hattori, and M. Watanabe, Improving the sensitivity of astronomical curvature wavefront sensor using dual-stroke curvature, *Publ. Astron. Soc. Pacific*. **120**, 655–664, (2008). doi: 10.1086/589755.
35. O. Guyon, High sensitivity wavefront sensing with a nonlinear curvature wavefront sensor, *Publ. Astron. Soc. Pacific*. **122**, 49–62, (2010). doi: 10.1086/649646.
36. D. Milman, D. Redding, and L. Needels, Analysis of curvature sensing for large-aperture adaptive optics systems, *J. Opt. Soc. Am. A*. **13**, 1226–1238, (1996). doi: 10.1364/JOSAA.13.001226.
37. M. van Dam and R. Lane, Extended analysis of curvature sensing., *J. Opt. Soc. Am. A*. **19**, 1390–1397, (2002). doi: 10.1364/JOSAA.19.001390.
38. M. van Dam and R. Lane, Wave-front sensing from defocused images by use of wave-front slopes., *Applied Optics*. **41**, 5497–5502, (2002). doi: 10.1364/AO.41.005497.